MODEL-BASED OPTIMIZATION OF PROCESS PARAMETERS IN HIGH ENERGY IMPACT ADDITIVE MANUFACTURING PROCESSES

THOMAS WILHELM[1*], LUKAS FUCHS[1*], ANTON MAKSAKOV[2,3], YANNIK SINNWELL[3], SERGIY ANTONYUK[3], STEFAN PALIS[2], VOLKER SCHMIDT[1]

[1] *Ulm University, Institute of Stochastics, Helmholtzstraße 18, 89069 Ulm, Germany*

[2] *Clausthal University of Technology, Institute for Electrical Information Technology, Adolph-Roemer-Straße 2A, 38678 Clausthal-Zellerfeld, Germany*

[3] *University of Kaiserslautern-Landau (RPTU), Institute of Particle Process Engineering, Gottlieb-Daimler-Straße 44, 67663 Kaiserslautern, Germany*

Abstract. Cold gas spraying is an emerging technology in additive manufacturing, known for its versatility and broad range of applications. This process enables the deposition of various materials, such as metals, ceramics and polymers, onto substrates by accelerating particles to high velocities within a Laval nozzle. To achieve optimal manufacturing quality at low cost, continuous and precise adjustment of process parameters is essential. However, due to the complex behavior of the gas dynamics, assessing quality during manufacturing is challenging. To address this issue, we describe and compare two data-driven modeling approaches that connect process parameters to particle descriptors within the spray jet: a fast and easy-to-implement radial basis function network (RBFN) method and a low-parametric copula-based method in order to probabilistically model the high-dimensional dependencies among particle descriptors. These two modeling approaches are illustrated through an example of data-based optimization of process parameters for a cold gas spray in free jet, but are directly applicable to non-free jet data, if available. Additionally, both methods have low computational cost, making them suitable for applications even in autonomous process control.

Keywords: additive manufacturing, vine copula, radial basis function network, model-based optimization, cold gas spray.

*these authors contributed equally.

1. Introduction

The cold gas spray process has, in recent decades, rapidly developed into an established method in additive manufacturing, enabling energy-efficient three-dimensional (3D) production [1, 2]. It is commonly used for surface coating, including corrosion protection, such as coating steel with copper or aluminum[3], minimization of material degradation [4], and widely employed in the field of repairing operations across various sectors [5–9]. In this process, particles dispersed in a heated inert gas stream (nitrogen or helium) are accelerated through a Laval nozzle to a velocity in $[200\,\mathrm{m\,s^{-1}}, 1000\,\mathrm{m\,s^{-1}}]$. Since the particles are heated well below their melting point in an inert gas, the method is especially suitable for oxygen-sensitive materials [10]. In addition, the cold gas spray process is not limited to layer-by-layer deposition of the sprayed material [11], but can be applied from any spray angle that can be adjusted during the manufacturing process [12].

The physical principles of this process are based on the cold gas process [6, 10, 13, 14]. When particles collide with a substrate material, a high-energy impact occurs, which leads to strong plastic deformation. The energy released in a short impact time causes a weld-like bond between the particle and substrate material, due to the mechanism of adiabatic shear instability [15]. The success of the particle bonding depends, in particular, on the impact velocity. Particle deposition occurs when a minimum velocity, the so-called critical velocity, is surpassed [16]. The critical velocity is a material-dependent quantity that is influenced by temperature, density and thermo-mechanical properties of both the particle and the substrate, described by the averaged tensile strength and the averaged melting temperature [16, 17]. The acceleration of particles to the critical velocities is an energy intensive process and accounts for a significant share of the energy consumption in gas spray systems. In the face of rising energy costs, it is important to increase the efficiency of energy use for gas spray systems on an industrial scale. Therefore, advanced model analysis of the acceleration behavior of particles in gas spray systems combined with optimization of energy performance is of high interest for practical applications.

Various models have been developed to estimate particle velocity within cold gas spray systems. One common approach utilizes simplified quasi-1D Euler equations to calculate an analytical steady-state solution for gas dynamics based on nozzle geometry. Particle acceleration is then determined using a drag force equation [18]. While this method accurately estimates average gas velocity, the presence of shock waves in supersonic regimes negatively impacts particle velocity estimation, often leading to significant overestimation. To address this issue, in [6, 19–21] an empirical equation for estimating particle velocity based on nozzle expansion ratio, gas temperature, and particle geometry was proposed. While these empirical models offer a broader applicability across various cold gas spray systems, they typically focus on predicting mean particle descriptors and do not reflect the distribution of particle velocities, sizes, and spread from the center of the jet plume which is necessary for a precise process quality prediction.

The present study focuses on optimizing process parameters of the particle-gas flow by introducing a modeling procedure of particle descriptors within the gas flow. More precisely, we model the multivariate probability distribution of particle velocity, spread, and size (particle diameter) as a function of two adjustable process parameters, namely the gas temperature and the distance between the substrate and the nozzle. Since there is a direct connection between the distribution of these particle descriptors and the process quality in terms of precision and fraction of bonded particles, a link between process parameters and process quality measures is achieved, and thus, a process parameter optimization is enabled. However, the measurement of particle behavior on impact is a challenging task as it requires the measurement device to be at the same position as the substrate, which is not feasible. Thus, as preliminary work, we concentrate on measurements conducted on particles in the free jet to circumvent this additional challenge. However, the proposed purely data-driven approaches for modeling particle descriptors can be easily generalized to a non-free jet setup.

In order to capture the complex dependencies between particle descriptors and process parameters, but also between the particle descriptors themselves, multivariate probabilistic modeling of particle descriptors is used. More precisely, two modeling approaches are described and compared. One of these approaches is based on so-called R-vine copulas, while the second one is based on radial basis functions. Vine copulas have been proven to be a

useful tool for hierarchical modeling of multivariate probability distributions of descriptor vectors in high dimension [22–24]. Hereby, parametric univariate and bivariate distributions are combined to construct the multivariate probability density function of a random vector in arbitrary dimension, leading to an efficient, low-parametric characterization of particle systems. An advantage of this model is that vine copulas inherently describe non-linear relationships between the influencing factors, i.e., we derive a relationship between adjustable process parameters and model parameters. The second modeling approach is based on a fast and easy-to-implement radial basis function network (RBFN) method [25], where RBFNs are artificial neural networks with one hidden layer that use radial basis functions as activation functions. This class of neural networks is widely used for function approximation [26, 27], classification [27] and probability density estimation [28]. Moreover, RBFNs are straightforward to use without requiring prior knowledge of the data, making them practical for various further applications. The RBFN modeling approach is used to directly model the multivariate probability distribution of particle descriptors and their changes with alternations in process parameters. The resulting multivariate distributions of particle descriptors are employed to predict process quality for given process parameters. Thereby, process quality is influenced by both process costs, which is determined by the chosen process parameters, and product quality, which is determined by the distribution of particle descriptors.

The rest of this paper is organized as follows. Section 2 introduces the cold gas spray process examined in this study. In paricular, in Section 2.2, the prediction of process quality based on the distribution of particle descriptors, specifically, velocity, spread and size of particles, is explained. A copula-based model of the multivariate distribution of these descriptors for given process parameters is then described in Section 2.3.1, followed by a description of the approach which uses RBFNs in Section 2.3.2. Section 3 provides the results of a comparative analysis of these two modeling approaches in terms of precision, applicability, and predicted optimal process parameters. Section 4 concludes and gives a short outlook to possible future research.

2. Materials and methods

In this section, we describe the materials and methods used in this work. It includes a detailed explanation of the additive manufacturing process in Section 2.1, which provides further details on the experimental setup of the cold gas spray process and how the particle descriptors were obtained. In particular, the measurement of particle velocity is crucial for the proposed process optimization framework by identifying optimal process parameters, as detailed in Section 2.2. In addition, the optimization approach requires modeling of the multivariate probability distribution of particle descriptors, for which two modeling approaches–copula-based and RBFNs—were employed, as stated in Section 2.3.

2.1. **Additive manufacturing process**

To begin with, we explain the cold gas spray which is considered in this paper as an additive manufacturing process. First, the cold gas spraying setup is described in Section 2.1.1. Then, in Section 2.1.2, we state how the particle velocity is tracked in the free jet.

2.1.1. ***Cold gas spraying setup.*** An in-house designed low-pressure cold gas spray system operates with nitrogen as a carrier gas up to a pressure of 12 bar [29–31]. The main components of the system are the pressurized aerosol generator, the electric heater and the Laval nozzle flange (Figure 1, center). The aerosol generation is performed by a dosing ring powder feeder (SAG 409, Topas GmbH) operated under system pressure for precise particle dispersion in the carrier gas. The Particles are conveyed from the feed hopper to the rotating dosing ring by a screw conveyor. The subsequent aerosol generation is realized by a Venturi nozzle mounted above the dosing ring, through which the carrier gas flows and extracts the particles from the dosing ring. The particle load of the carrier gas can be controlled by adjusting the rotational speed of the dosing ring and the rotation speed of the screw conveyor. Copper powder produced by gas atomization process (Sigma Aldrich, Copper-powder (spheroidal) 98%) in the size range of 5-30 µm is used as the particle material (Figure 1, left). The aerosol is heated via an externally heated electric tube

heater directly connected to the nozzle, where the heated aerosol is compressed. An optimized Laval nozzle design is used to achieve optimal particle exit velocity for particles in the size range of 1-25 µm [31]. The nozzle comprises a cylindrical inlet, as well as divergent and convergent sections, with a height of 30 mm and a diameter of 10 mm. It has a throat diameter of 0.8 mm and an outlet cross-section of 1.5 mm. Due to the low throat diameter and outlet cross-section, the nozzle belongs to the category of micro nozzles and enables high manufacturing precision.

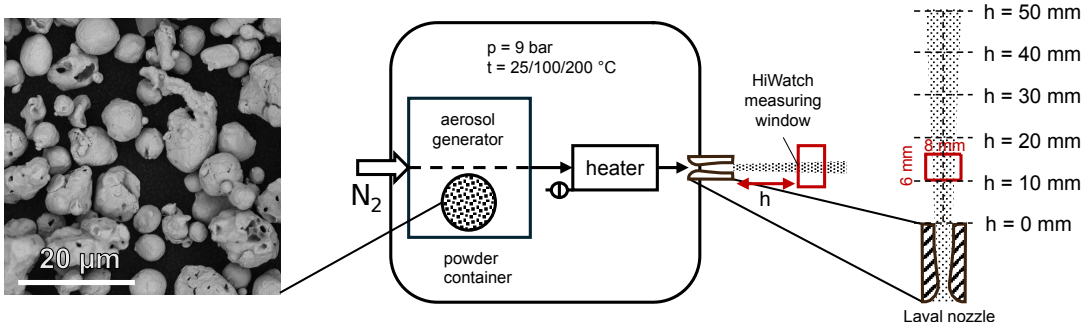

FIGURE 1. Schematic representation of the cold gas spray process (center) with a scanning electron microscopy (SEM) image of the feed stock powder (left). Representation of the H-PIV measuring sequence with variation of the measuring window position in the nozzle jet (right).

2.1.2. ***Particle tracking velocimetry.*** To characterize the spraying process, a high-speed particle image velocimetry (H-PIV) instrument (Oseir Hiwatch HR2) is used (Figure 2a) [32]. The focal plane of this device is positioned in relation to the center of the jet plume. The system allows the quantification of the particle velocity $v \leq 2000\,\mathrm{m\,s^{-1}}$, the particle diameter $d \in [5\,\mu\mathrm{m}, 200\,\mu\mathrm{m}]$ and spread $s \in [-4\,\mathrm{mm}, 4\,\mathrm{mm}]$ as the position deviation from the center of the jet plume, thus providing a basis for the characterization of the spraying process. The detection of particle velocity and spread is based on the shadowing of laser pulses (pulse duration of 80 ns and a pulse intervall length of 800 ns). If aerosol particles are moving within the measurement plane (8 mm × 6 mm) after leaving the nozzle, triplets of the particle movement can be recorded by adjusting the laser pulse duration and frequency. Particle velocity is computed from the distance traveled, knowing the time interval between each triplet recorded with appropriate signal-to-noise ratio. An example of a pair of non-processed and processed camera outputs is visualized in Figure 2b.

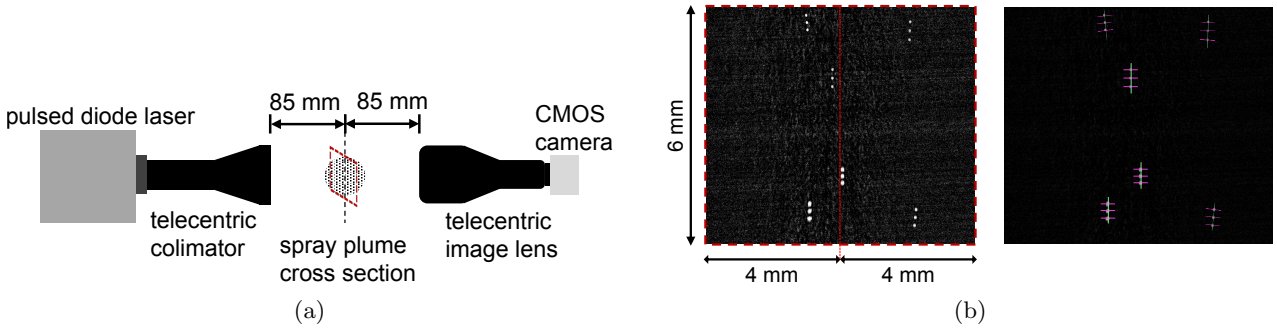

FIGURE 2. Illustration of the optical measurement principle of the HiWatch HR2 based on laser pulses and tracking of shadowing by passing particles (a), where a live image of the measurement area with the characteristic particle triplets is shown (b, left), as well as a processed image with particle tracking (b, right). The center of the jet plume is shown as a red line (b,left).

2.1.3. ***Data acquisition.*** In this work, two adjustable process parameters that influence the particle velocity are taken into account in the control of the cold gas spray process. The temperature $t \geq 25\,^{\circ}\mathrm{C}$ of the aerosol before it enters the Laval nozzle and the distance $h \geq 0\,\mathrm{mm}$ between the substrate surface and the nozzle outlet can be adjusted. In order to quantify the relationship between process parameters and particle descriptors, an experimental parameter variation is carried out. The experiments were conducted at a constant carrier gas pressure of 9 bar at the nozzle inlet while varying training data acquisition the process gas temperature $t = 25\,^{\circ}\mathrm{C}$, $100\,^{\circ}\mathrm{C}$, $200\,^{\circ}\mathrm{C}$ and varying the distance of the nozzle to the velocimetry $h = 0\,\mathrm{mm}, 10\,\mathrm{mm}, \ldots, 50\,\mathrm{mm}$. In the following, we refer to the set of tuples of process parameters for which measurements are available as $\mathcal{M}$, i.e., $\mathcal{M} = \{25, 100, 200\} \times \{0, 10, \ldots, 50\}$. Furthermore, an additional experiment with gas temperature of $t = 75\,^{\circ}\mathrm{C}$ and distance of $h = 15\,\mathrm{mm}$ to the velocimetry has been performed for model validation.

Note that $h = 0\,\mathrm{mm}$ does not represent a camera positioned directly at the nozzle outlet, but rather the closest feasible position allowed by the process setup. In fact, centering the measurement device exactly at the nozzle exit would correspond to approximately $h \approx -5\,\mathrm{mm}$. In the current configuration, a minimal distance of 2 mm from the nozzle is maintained due to the presence of a steel cap used to secure the nozzle. Additionally, the HiWatch camera has a measurement window size of 6 mm. The acquired datasets are used to calibrate the proposed process modeling approaches. To eliminate errors resulting from imperfect centering of the measurement device, for each measurement the particle spreads are centered by subtracting their arithmetic mean. Additionally, based on the assumption of symmetric particle spread within the jet, the measurements are mirrored at the cone's center to expand the dataset. The numbers of particles observed in the individual experiments are listed in Table 1, see Section 3 below.

2.2. **Process optimization**

To classify a particle observed in the data as bonding to being bonded to the substrate after collision, the concept of critical velocity is utilized. A particle is considered bonded if its velocity exceeds a certain threshold, known as the critical velocity, $v_{\mathrm{crit}} > 0\,\mathrm{m\,s^{-1}}$. In the present paper, we use the model of critical velocity proposed in [33], which is given by

$$v_{\mathrm{crit}}(t, d) = k_1 \frac{\sqrt{657000 - 600 \cdot (t + 273.15)}}{d^{0.18}} \tag{1}$$

for a particle with temperature t in °C and diameter d in µm, where the factor 273.15 accounts for the conversion between Celsius and Kelvin. In [34] it was reported that v_{crit} depends on the combination of particle material and substrate. Therefore, the expression for v_{crit} was derived specifically for copper particles, with the coefficient k_1 accounting for the variations in substrate materials and being heuristically set equal to 0.8.

The product quality in cold gas spraying is primarily determined by two factors: a high fraction of particles successfully bonding to the substrate in order to minimize process time and material waste, and low particle spread in order to achieve a precise layer formation. Here, we define the product quality of a spraying experiment with process parameter vector (t, h) as the ratio $\delta_{p_{\max}}(x^{(t,h)})$ of the volume of bonded particles with small deviation from the center of the jet plume to the total particle volume, which is given by

$$\delta_{p_{\max}}(x^{(t,h)}) = \frac{\sum_{i=1}^{n^{(t,h)}} d_i^3 \mathbb{1}_{[v_{\mathrm{crit}}(t,d),\infty)}(v_i) \mathbb{1}_{[0,p_{\max}]}(|s_i|)}{\sum_{i=1}^{n^{(t,h)}} d_i^3}, \tag{2}$$

where $\mathbb{1}_A$ denotes the indicator of a set $A \subset \mathbb{R}$, i.e., $\mathbb{1}_A(x) = 1$ if $x \in A$, otherwise $\mathbb{1}_A(x) = 0$. The set $x^{(t,h)}$ denotes a sample of $n^{(t,h)}$ particle descriptor vectors observed by image measurements and is given by

$$x^{(t,h)} = \left\{ x_i^{(t,h)}, i = 1, \ldots, n^{(t,h)} \right\}, \tag{3}$$

where the vector $x_i^{(t,h)} = (v_i, s_i, d_i)$ contains the velocity, spread and diameter of the ith particle. Furthermore, $p_{\max}$ describes the maximum desired spread of particles. Note that maximizing the value of the ratio $\delta_{p_{\max}}(x^{(t,h)})$ given

in Eq. (2) accounts for both, particles that do not exceed the critical velocity, and particles that have a larger spread than $p_{\max}$.

When considering industrial-scale process optimization, not only the quality of the product, but also the costs of the process has to be taken into account. The costs of the considered process are dominated by heating costs, which are assumed to increase quadratically with temperature. This results in the process quality measure $\eta_{p_{\max},\alpha}(x^{(t,h)}, t)$, which is given by

$$\eta_{p_{\max},\alpha}(x^{(t,h)}, t) = \delta_{p_{\max}}(x^{(t,h)}) - (\alpha t)^2, \tag{4}$$

where α is a coefficient that models the heating cost per 1°C. The function given in Eq. (4) is easily interpretable and computationally efficient; however, it relies on a limited number of measured particle descriptors instead of their underlying distribution. Thus, to be more robust and to account for the underlying probability distribution of particle descriptor vectors, the expression in Eq. (4) is transformed into an objective function $R\colon \mathcal{T} \times \mathcal{H} \to \mathbb{R}$, by considering the distribution of particle descriptors vectors rather than its realizations, where

$$R(t,h) = \frac{\int_0^\infty \int_{-\infty}^\infty \int_0^\infty d^3 f_{(V,S,D)}^{(t,h)}(v,s,d)\, \mathbb{1}_{[v_{\text{crit}}(t,d),\infty)}(v)\, \mathbb{1}_{[0,p_{\max}]}(|s|)\, \mathrm{d}v\, \mathrm{d}s\, \mathrm{d}d}{\int_0^\infty \int_{-\infty}^\infty \int_0^\infty d^3 f_{(V,S,D)}^{(t,h)}(v,s,d)\, \mathrm{d}v\, \mathrm{d}s\, \mathrm{d}d} - (\alpha t)^2, \tag{5}$$

and $f_{(V,S,D)}^{(t,h)}(v,s,d)$ denotes the joint probability density of particle velocity v, spread s, and size d for a given process parameter vector (t,h). Here, the set $\mathcal{T} \times \mathcal{H} = [25\,°\text{C}, 200\,°\text{C}] \times [0\,\text{mm}, 50\,\text{mm}]$ is the set of admissible process parameters. The goal is to find an optimal vector of process parameters $(t^*, h^*) \in \mathcal{T} \times \mathcal{H}$ which maximizes the value of $R(t,h)$. To achieve this goal, the probability density $f_{(V,S,D)}^{(t,h)}(v,s,d)$ of particle descriptor vectors will be modeled in two different way, see Section 2.3 for details.

2.3. **Process modeling**

The basic idea in order to model the particle descriptor vectors consisting of particle velocity, spread, and diameter is to view these vectors as realizations of a random vector $(V^{(t,h)}, S^{(t,h)}, D^{(t,h)})$ for each vector $(t,h) \in \mathcal{T} \times \mathcal{H}$ of admissible process parameters. A realization $(v^{(t,h)}, s^{(t,h)}, d^{(t,h)})$ of $(V^{(t,h)}, S^{(t,h)}, D^{(t,h)})$, belonging to the set $\mathcal{X} = (0,\infty) \times \mathbb{R} \times (0,\infty)$, can be interpreted as descriptor vector of a single particle that is observed via image measurement during the spraying process, where $v^{(t,h)}$ is measured in $\text{m}\,\text{s}^{-1}$, $s^{(t,h)}$ in mm and $d^{(t,h)}$ in µm. Recall that in each spraying experiment with temperatures $t = 25\,°\text{C}, 100\,°\text{C}, 200\,°\text{C}$ and distances $h = 0\,\text{mm}, 10\,\text{mm}, \ldots, 50\,\text{mm}$, a sample of particle descriptor vectors is obtained. Based on these samples we seek for the multivariate probability density $f_{(V,S,D)}^{(t,h)}\colon \mathcal{X} \to [0,\infty)$ of $(V^{(t,h)}, D^{(t,h)}, S^{(t,h)})$, for each vector $(t,h) \in \mathcal{T} \times \mathcal{H}$.

There are several tools for multivariate density estimation, including kernel density estimators [35], Gaussian mixture models [36], and neural network-based density estimators [28]. However, these models often struggle with interpolation between probability densities. Most approaches only allow pointwise interpolation within the probability density regime, which can lead to undesirable artifacts, such as inconsistency in modality. For instance, interpolating between two unimodal probability densities can result in an artificial bimodal distribution. To overcome this problem, a parametric, copula-based modeling approach [22, 37, 38] is presented in Section 2.3.1. Copulas are a suitable tool to model multivariate probability distributions by first modeling the (univariate) marginal distributions and then, subsequently, modeling their pairwise dependency structure. Due to the low-parametric nature of this modeling procedure, an interpolation of model parameters within the set $\mathcal{T} \times \mathcal{H}$ of admissible process parameter vectors (t,h) is possible, which allows for computing the density $f_{(V,S,D)}^{(t,h)}$ for unobserved process parameter vectors $(t,h) \notin \mathcal{M}$.

On the other hand, note that the parametric, copula-based modeling of the desired multivariate probability density $f_{(V,S,D)}^{(t,h)}$ does come with the costs of model assumptions. For example, the univariate densities $f_V^{(t,h)}$ $f_S^{(t,h)}$, and $f_D^{(t,h)}$ of the single (random) particle descriptors V, S, D, respectively, must belong to the same parametric family

of probability densities for each $(t, h) \in \mathcal{T} \times \mathcal{H}$. While this assumption holds in the case considered in the present paper, it could lead to issues in other applications. Thus, we still introduce an alternative modeling approach by means of radial basis function networks (RBFNs). This non-parametric approach does not require any assumptions regarding the marginal distributions or the interdependencies of V, S, D, offering greater flexibility at the expense of precision and the danger of overfitting. Moreover, RBFNs are differentiable functions, enabling efficient optimization via gradient-based methods. In Section 2.3.2, RBFNs are introduced in greater detail, along with the methodology used to predict multivariate probability densities.

2.3.1. ***Copula-based modeling.*** In this section, a more detailed explanation of parametric methods is presented for modeling both, the distribution of single particle descriptors by suitably chosen univariate probability densities, and the distribution of pairs of particle descriptors using a parametric copula-based approach. In the following, the parametric methods are described with respect to a sample of n particle descriptor vectors $x = \{x_i, i = 1, \dots, n\}$, where the vector $x_i = (v_i, s_i, d_i)$ contains the velocity, spread and diameter of the ith particle.

Univariate densities. First, marginal distributions are fitted for each single particle descriptor. In particular, the univariate probability densities f_V and f_D of particle velocity V and diameter D are estimated. On the other hand, regarding particle spread S, it is assumed that the deviation of the particles from the center of the spray plume is symmetrical to the center, since the jet plume is considered a cone. Therefore, we model the distribution of the absolute value $|S|$ of S. In this way, we obtain the univariate probability density $f_{|S|}$ of the absolute spread. Each of these three density functions is determined by the frequency of encountering values of the corresponding particle descriptor across the samples. From these observed frequencies, we obtain a parametric model by fixing a class of probability distributions per descriptor and subsequently fitting the parameters of the corresponding univariate probability distributions to the observed frequencies using maximum likelihood estimation [39]. For reduction of complexity, we assume that the marginal distributions can be modeled by two-parametric probability densities listed in [40].

Multivariate copula-based densities. The trivariate probability density $f_{(V,S,D)}$ is modeled by a parametric density function $f_\theta \colon \mathcal{X} \to [0, \infty)$, where $\theta \in \Theta$ and $\Theta \subseteq \mathbb{R}^9$ is some set of admissible model parameters. The nine components of the model parameter vector θ result from the fact that each marginal distribution has two parameters, and three further parameters will be considered for modeling the dependency of the particle descriptors using copulas. More precisely, according to Sklar's theorem [41], for each $(v, s, d) \in \mathcal{X}$ we put

$$f_\theta(v, s, d) = \frac{1}{2} c_{\theta_c}(F_{V,\theta_V}(v), F_{|S|,\theta_{|S|}}(|s|), F_{D,\theta_D}(d_D)) f_{V,\theta_V}(v) f_{S,\theta_{|S|}}(|s|) f_{D,\theta_D}(d), \tag{6}$$

where $\theta = (\theta_V, \theta_{|S|}, \theta_D, \theta_c) \in \Theta$ and $F_V, F_{|S|}, F_D$ denote the cumulative distribution functions of the densities $f_V, f_{|S|}, f_D$ with parameter vectors $\theta_V, \theta_{|S|}, \theta_D \in \mathbb{R}^2$, respectively. Furthermore, the function $c \colon [0,1]^3 \to [0, \infty)$ appearing in Eq. (6) is a copula density with parameter vector $\theta_c \in \mathbb{R}^3$. The factor $1/2$ comes from normalization, as we model the distribution of the absolute spread $|S|$ assuming that the distribution of the (centered) spread S itself is symmetrical about 0.

Note that the expression on the right-hand side of Eq. (6) is the product of a trivariate copula density and three univariate densities. However, the copula density c in Eq. (6) can be decomposed further such that the joint density f_θ of the three-dimensional random vector (V, S, D) is represented by a product of univariate and bivariate density functions only. This procedure for the factorization of multivariate probability densities is called the pair-copula construction method [42]. It involves applying the chain rule for conditional density functions, recursively expressing each conditional probability density by some (conditional) bivariate densities and decomposing each bivariate probability density using a bivariate copula density.

In order to determine all univariate and bivariate densities necessary for the pair-copula construction method, an appropriate structure for the decomposition mentioned above is needed, which is obtained by means of a graph

representation with trees. More precisely, so-called regular vine (R-vine) trees are used for the underlying structure. A particular choice of bivariate copulas for each pair in this decomposition is referred to as an R-vine copula. For more details regarding the construction of R-vine tree representations, we refer e.g., to [24]. To select a suitable vine structure and a family of bivariate copula densities, the sequential algorithm stated in [37] is used, where parametric families of Archimedean copulas (of Frank, Joe, Clayton and Gumbel type), and their rotations by 90, 180 and 270 degrees, are chosen as candidates for pair copulas. The parameters of these copulas are determined through maximum likelihood estimation [38].

In our application, the probability density $f^{(t,h)}_{(V,S,D)}$ for a sample of particle descriptor vectors $x^{(t,h)}$ with process parameter vector $(t,h) \in \mathcal{M}$ is modeled by means of Eq. (6), where we denote parameter vector of the copula-based model by $\theta^{(t,h)}$. An overview of this copula-based modeling procedure for multivariate probability densities is given in Figure 3.

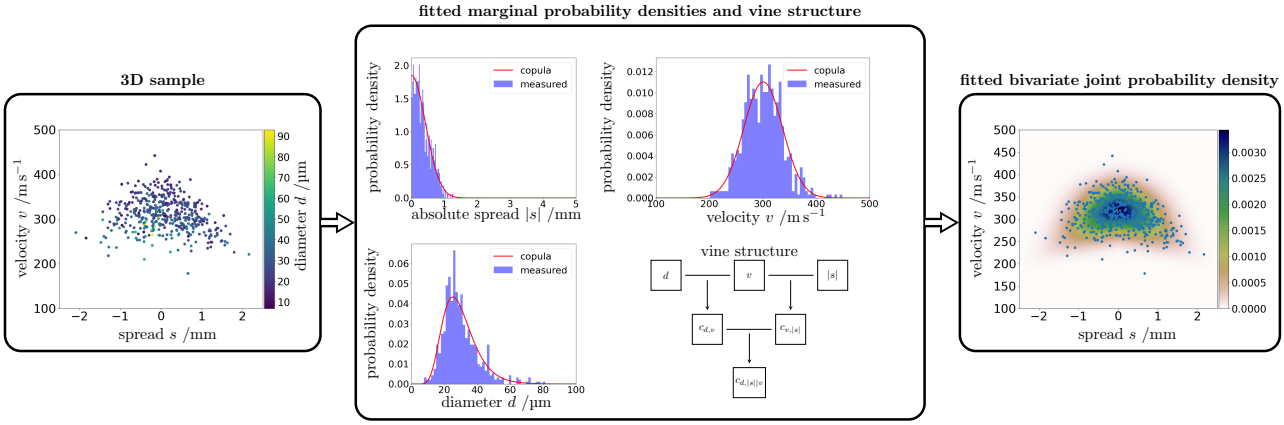

FIGURE 3. Graphical overview of the copula-based modeling procedure: Sample of the random particle descriptor vector (V,S,D) for a given vector (t,h) of process parameters (left). Fitting of univariate probability densities for absolute spread $|S|$, velocity V and diameter D, together with an R-vine tree representation of the trivariate probability density $f^{(t,h)}_{(V,S,D)}$ (center). Visualization of the resulting model for the bivariate probability density $f^{(t,h)}_{(V,S)}$, integrated over the particle diameter for visualization purposes (right).

Interpolation within the space of process parameters. The parametric modeling approach described above does not directly enable the prediction of a probability density $f^{(t,h)}_{(V,S,D)}$ for $(t,h) \notin \mathcal{M}$. For this purpose we assume that, for all process parameter vectors $(t,h) \in \mathcal{T} \times \mathcal{H}$, the densities $f_{\theta^{(t,h)}}$ have common types of marginal (univariate) densities for each particle descriptor as well as a common R-vine tree representation and common bivariate copula families. This structure of the densities $f_{\theta^{(t,h)}}$ given in Eq. (6) will be denoted by $Z \in \mathcal{Z}$, where $\mathcal{Z}$ is considered as the cross product of the sets of all admissible families of marginal distributions, R-vine tree representations and families of bivariate copula distributions as specified above. For more details, we refer to [22].

In the following for a given structure $Z \in \mathcal{Z}$, we will denote the densities $f_{\theta^{(t,h)}}$ by $f^{Z}_{\theta^{(t,h)}}$, computing the best-fitting model parameter vector $\widehat{\theta}^{(t,h)}_{Z}$ of $f^{Z}_{\theta^{(t,h)}}$ for each process parameter vector $(t,h) \in \mathcal{M}$ by maximum likelihood estimation [38]. More precisely, the vector $\widehat{\theta}^{(t,h)}_{Z}$ is obtained by maximizing the loglikelihood function $L^{(t,h)}_{Z} : \Theta \to \mathbb{R}$, which is given by

$$L^{(t,h)}_{Z}(\theta) = \sum_{(v,s,d) \in x^{(t,h)}} \log(f^{Z}_{\theta}(v,s,d)) \tag{7}$$

for each $\theta \in \Theta$, where $x^{(t,h)}$ denotes the sample of particle descriptor vectors (see Eq. (3)) and f_θ^Z is the probability density given by means of Eq. (6) with structure $Z \in \mathcal{Z}$. In a second optimization step, given the optimal model parameter vectors $\widehat{\theta}_Z^{(t,h)}$ for each structure $Z \in \mathcal{Z}$, an optimal structure $\widehat{Z} \in \mathcal{Z}$ is computed. This is done by maximizing a weighted mean of the loglikelihoods $L_Z^{(t,h)}(\widehat{\theta}_Z^{(t,h)})$ given in Eq. (7), over all process parameter vectors $(t,h) \in \mathcal{M}$. Note that a weighted mean is considered due to the different numbers $n^{(t,h)}$ of particles observed for each of the process parameter vectors $(t,h) \in \mathcal{M}$ (see Table 1), which strongly influence the values of $L_Z^{(t,h)}(\widehat{\theta}_Z^{(t,h)})$. The overall best structure $\widehat{Z} \in \mathcal{Z}$ is therefore provided by

$$\widehat{Z} = \arg\max_{Z \in \mathcal{Z}} \frac{1}{\#\mathcal{M}} \sum_{(t,h) \in \mathcal{M}} \frac{1}{n^{(t,h)}} L_Z^{(t,h)}(\widehat{\theta}_Z^{(t,h)}), \tag{8}$$

where $\#\mathcal{M}$ denotes the cardinality of the set $\mathcal{M}$.

The restriction to a common structure $\widehat{Z} \in \mathcal{Z}$ enables the interpolation within the space of process parameters to model the probability density $f_{(V,S,D)}^{(t,h)}$ for each $(t,h) \in \mathcal{T} \times \mathcal{H}$. More precisely, a function $\lambda\colon \mathcal{T} \times \mathcal{H} \to \Theta$ is used to predict the model parameter vector for vectors of process parameters for which no measurements are conducted so far. Thus, for each $(t,h) \in \mathcal{T} \times \mathcal{H}$, the density $f_{(V,S,D)}^{(t,h)}$ is modeled by the function $f_\theta^{\widehat{Z}}\colon \mathcal{X} \to [0,\infty)$ introduced in Eq. (6), where the model parameter vector $\theta \in \Theta$ is given by $\theta = \lambda(t,h)$ and $\widehat{Z} \in \mathcal{Z}$ is the common structure of $f_{\lambda(t,h)}^{\widehat{Z}}$ for all $(t,h) \in \mathcal{T} \times \mathcal{H}$. The components of λ are assumed to be polynomials of degree 2, i.e., $\lambda = (\lambda_1, \ldots, \lambda_9)$ and

$$\lambda_k(t,h) = \sum_{i=0}^{2} \sum_{j=0}^{2} a_{ijk}\, h^i t^j, \tag{9}$$

for any $k \in \{1, \ldots, 9\}$ and $(t,h) \in \mathcal{T} \times \mathcal{H}$. The coefficients a_{ijk} in Eq. (9) are determined by the least squares fit (see [43]) to the optimal model parameter vectors $\widehat{\theta}_{\widehat{Z}}^{(t,h)}$ fitted for the process parameter vectors $(t,h) \in \mathcal{M}$ and the common structure $\widehat{Z} \in \mathcal{Z}$. For an illustration of the interpolation approach stated above, see Figure 4.

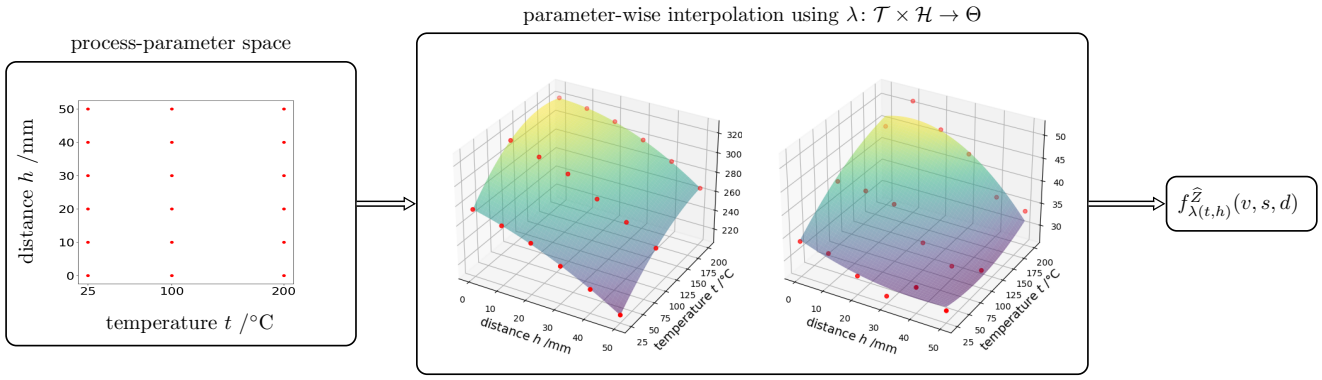

FIGURE 4. Illustration of the interpolation approach within the parameter space: Sample of process parameters for which measurements are available (left). Interpolation within the space of process parameters using the function $\lambda\colon \mathcal{T} \times \mathcal{H} \to \Theta$ to obtain the probability density $f_{\lambda(t,h)}^{\widehat{Z}}$ for any $(t,h) \in \mathcal{T} \times \mathcal{H}$, where two components λ_i, λ_j of λ are visualized as surface plots (center).

2.3.2. ***RBFN-based modeling.*** Radial basis function networks (RBFNs) are nonlinear regression models, which inherit a neural network architecture with one hidden layer of $N > 0$ perceptrons and a radial basis function as

activation function [25]. In this work, we use a RBFN of the form $g_{\theta_{\mathrm{RBF}}} : \mathcal{T} \times \mathcal{H} \times \mathcal{X} \to [0, \infty)$, where $\theta_{\mathrm{RBF}} \in \widetilde{\Theta}$ and $\widetilde{\Theta} \subseteq \mathbb{R}^{6N+1}$ is some set of admissible model parameters, to model the trivariate probability density $f^{(t,h)}_{(V,S,D)}$ for each process parameter vector $(t, h) \in \mathcal{T} \times \mathcal{H}$. The values of the function $g_{\theta_{\mathrm{RBF}}}$ are given by

$$g_{\theta_{\mathrm{RBF}}}(t, h, v, s, d) = \sum_{i=1}^{N} w_i \varphi_{\sigma,\mu_i}(t, h, v, s, d) \quad \text{with } \varphi_{\sigma,\mu_i}(y) = \frac{1}{(\sqrt{2\pi}\sigma)^5} \exp^{-0.5(\frac{\|y-\mu_i\|}{\sigma})^2} \tag{10}$$

for each $(t, h, v, s, d) \in \mathcal{T} \times \mathcal{H} \times \mathcal{X}$, where $\|y - \mu_i\|$ denotes the Euclidean norm of $y - \mu_i \in \mathbb{R}^5$ and $\varphi_{\sigma,\mu_i} \colon \mathbb{R}^5 \to (0, \infty)$ is the normalized Gaussian kernel with mean $\mu_i \in \mathbb{R}^5$ and standard deviation $\sigma > 0$. Furthermore, the scaling factors $w_i \in \mathbb{R}$ for $i \in \{1, \ldots, N\}$ determine the contribution of each kernel to $g_{\theta_{\mathrm{RBF}}}$. Thus, the model parameter vector $\theta_{\mathrm{RBF}} \in \widetilde{\Theta}$ of $g_{\theta_{\mathrm{RBF}}}$ is given by $\theta_{\mathrm{RBF}} = (w_1, \ldots, w_N, \mu_1, \ldots, \mu_N, \sigma)$.

Note that by selecting the weights w_i in Eq. (10) to be non-negative and such that $\sum_{i=1}^{N} w_i = 1$, the function $g_{\theta_{\mathrm{RBF}}}$ given in Eq. (10) is a probability density as a convex combination of probability densities. The probability density $f^{(t,h)}_{(V,S,D)}$ is then modeled by conditioning $g_{\theta_{\mathrm{RBF}}}$ on $(t, h) \in \mathcal{T} \times \mathcal{H}$, i.e., we put

$$f^{(t,h)}_{(V,S,D)}(v, s, d) = \frac{g_{\theta_{\mathrm{RBF}}}(t, h, v, s, d)}{\int_0^\infty \int_{-\infty}^\infty \int_0^\infty g_{\theta_{\mathrm{RBF}}}(t, h, v, s, d) \, \mathrm{d}v \, \mathrm{d}s \, \mathrm{d}d} \tag{11}$$

for any $(v, s, d) \in \mathcal{X}$ and for each process parameter vector $(t, h) \in \mathcal{T} \times \mathcal{H}$. There may not be a noteworthy interpretation of the probability distribution of t and h, as these quantities are determined by the choice of process parameters used in data acquisition. Nevertheless, the RBFN-based modeling approach offers the advantage that the RBFN is trained to model the probability density $f^{(t,h)}_{(V,S,D)}$ not only for a single vector $(t, h) \in \mathcal{T} \times \mathcal{H}$ of process parameters, but for all vectors from $\mathcal{T} \times \mathcal{H}$ simultaneously, i.e., no additional interpolation is needed.

The best-fitting model parameter vector $\widehat{\theta}_{\mathrm{RBF}} \in \widetilde{\Theta}$ is obtained by maximum loglikelihood estimation [38]. More precisely, the vector $\widehat{\theta}_{\mathrm{RBF}}$ minimizes the negative loglikelihood function $\widetilde{L} \colon \widetilde{\Theta} \to \mathbb{R}$, which is given by

$$\widetilde{L}(\theta_{\mathrm{RBF}}) = - \sum_{(t,h) \in \mathcal{M}} \sum_{(v,s,d) \in x^{(t,h)}} \log(g_{\theta_{\mathrm{RBF}}}(t, h, v, s, d)), \tag{12}$$

where $x^{(t,h)}$ is the sample of particle descriptor vectors measured for the process parameter vector $(t, h) \in \mathcal{M}$, see Section 2.2. The minimization of the expression given in Eq. (12) is performed by gradient descent using an Adam optimizer [44] with a learning rate of 0.01. Note that, in order to achieve better results, the data were normalized before used in training, i.e., the values of all process parameters as well as particle descriptors are first centered by subtracting their arithmetic mean and then normalized by dividing by their empirical standard deviation. To determine the optimal number N of perceptrons, we employ leave-one-out cross-validation [45]. In particular, we set $N \in \{1, \ldots, 50\}$ to remain within reasonable computational time. An illustration of the RBFN-based modeling procedure is given in Figure 5.

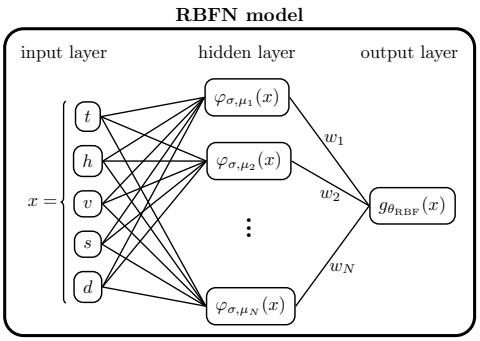

FIGURE 5. Neural network architecture of the RBFN-based modeling approach: The network input consists of a vector, containing both, process parameter vector $(t, h) \in \mathcal{T} \times \mathcal{H}$ and particle descriptor vector $(v, s, d) \in \mathcal{X}$.

3. Results and discussion

In Section 2.3, two different approaches have been stated to model the trivariate probability density $f^{(t,h)}_{(V,S,D)}$ of each process parameter vector $(t, h) \in \mathcal{T} \times \mathcal{H}$. These models are deployed to implicitly estimate product quality by means of an objective function and thus enable process parameter optimization, see Section 2.2. However, it is worth noting that modeling the distribution of particle descriptors has way more advantages. For instance, this enables the investigation of potential increase of process quality by a change in the particle size distribution, i.e., using another particle system. Furthermore, our modeling approaches can be used to investigate the causes of low product quality, such as identifying factors contributing to a low objective function, e.g., whether due to insufficient particle velocity or excessive particle spread. Additionally, it facilitates estimation of the spatial distribution of particle mass that bonds to the substrate, providing valuable insight for process enhancement, besides the information aggregated in the objective function. Before investigating this in Section 3.2 in more detail, the strengths and weaknesses of the two modeling approaches are discussed in Section 3.1.

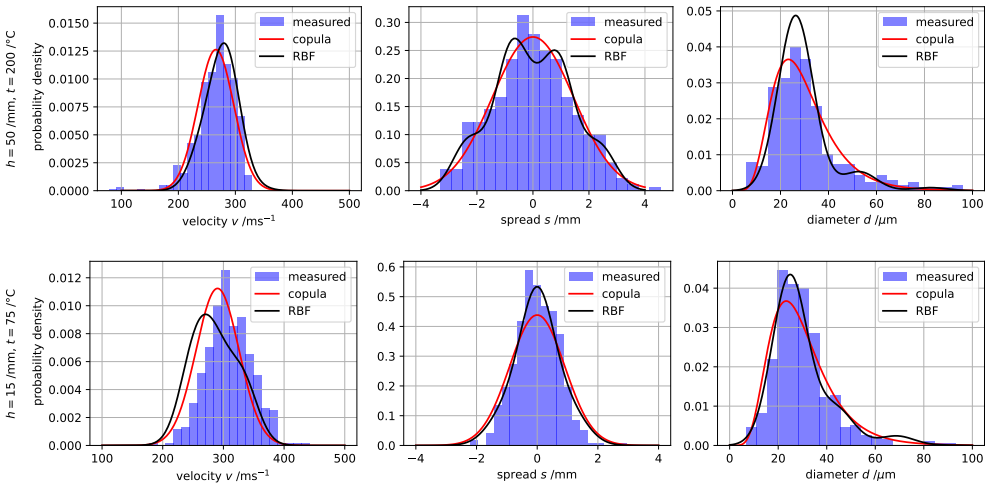

FIGURE 6. Univariate probability densities of V, S and D for two different process parameter vectors (t, h), obtained by the copula-based (red) and RBFN-based (black) model. Measured data is represented by normalized histograms (blue). The top row corresponds to data used for training, while the bottom row displays the validation dataset.

3.1. **Evaluation of modeling approaches**

For the copula-based modeling approach explained in Section 2.3.1, we determined the following families of univariate (marginal) probability densities, R-vine copula structure and corresponding families of bivariate copula densities. Velocity V and diameter D of particles are modeled by normal and lognormal distributions, respectively, whereas the absolute particle spread $|S|$ is modeled by a truncated normal distribution on the interval $[0, \infty)$. The R-vine structure is chosen such that the correlation between V and D is modeled by a Clayton copula with 90° rotation, and the correlation between V and S by a Clayton copula with 270° rotation, while the conditional bivariate copula density is given by means of a Joe copula with 90° rotation. In this way, we get a model $\{f^{\widehat{Z}}_{\lambda(t,h)}, (t,h) \in \mathcal{T} \times \mathcal{H}\}$ for the trivariate probability densities of (V, S, D), which has $81 = 9 \cdot 9$ parameters. For the RBFN-based modeling approach stated in Section 2.3.2, the choice of the number N of radial basis functions, i.e., the number of perceptrons in the RBFN, heavily influences model complexity and the risk of overfitting, where the value of N was determined as $N = 30$, by considering cross validation. This results in $181 = 30 \cdot (5 + 1) + 1$ trainable parameters.

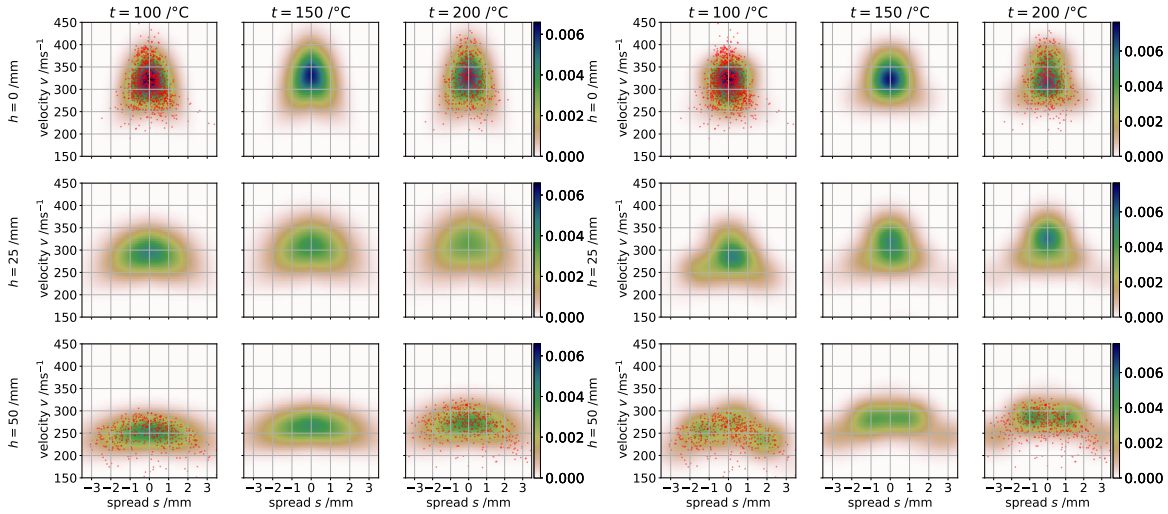

FIGURE 7. Bivariate density of (V, S) for different process parameter vectors (t, h): for the copula model (left) and the RBFN model (right). Measured data points, where available, are shown in red.

In Figure 6, the resulting marginal distributions of both modeling approaches, along with the corresponding data for two process parameter vectors, are displayed. Note that the second row in Figure 6 corresponds to process parameters not used for model calibration. Additionally, Figure 7 illustrates the bivariate densities of (V, S) for four process parameter vectors $(t, h) \in \mathcal{M}$ within the training set (together with visualized training data) and five process parameter vectors $(t, h) \notin \mathcal{M}$ outside the training data. It is clearly visible how the restrictions of the copula-based model, specifically the choice of marginal distribution families and copula families, result in both unimodal univariate and bivariate distributions. Conversely, the RBFN-based approach often yields multimodal distributions, as seen, for instance, in Figure 7 for $h = 50\,\text{mm}$ and $t = 100\,°\text{C}$. Moreover, the particle spread S, which is assumed to be symmetrically distributed around zero, is often asymmetrically modeled by the latter approach, see Figure 6 (second column) and Figure 7. For the copula model, the densities $f^{\widehat{Z}}_{\lambda(t,h)}$ for $(t, h) \in \mathcal{T} \times \mathcal{H} \setminus \mathcal{M}$ are obtained by parameter-wise interpolation, resulting in a smooth transition of distribution shapes across variations of process parameter

vectors while preserving key shape descriptors, such as unimodality and symmetry. Furthermore, note that the copula-based modeling approach is much more resistant to overfitting if the training datasets include measurements with errors due to a non-ideal or inconsistent experimental setup. Anyhow, also the RBFN model exhibits quite good fits to training data and provides reasonable results for validation data which have not been used for model calibration, see Figure 6 (bottom row). In terms of computational efficiency, the RBFN model shows an advantage. The time necessary for evaluating the trivariate probability density $f^{(t,h)}_{(V,S,D)}$ of the RBFN model is significantly lower than that of the copula model. More precisely, the evaluation of the RBFN-based probability density $f^{(t,h)}_{(V,S,D)}(v,s,d)$ (see Eq. (11)) at a vector $(t,h,v,s,d) \in \mathcal{T} \times \mathcal{H}$ takes $9 \cdot 10^{-8}$s, whereas the evaluation of the copula-based probability density (see Eq. (6)) takes $5 \cdot 10^{-7}$s.

In Table 1, the expected particle velocity $\mathbb{E}S$ as well as descriptors of product quality obtained from both (copula and RBFN) models are compared with corresponding quantities observed for measured training and validation data. Note that a clear trend to higher accuracies can be observed for the copula model, however, the prediction quality of the RBFN model is high as well.

TABLE 1. For given process parameters (t,h), the number of particles (# particles) observed in measured data is shown, as well as the expected particle velocities obtained for measured data and both (copula and RBFN) models. In addition, for $\alpha = 0$ and $p_{\max} = 0.5$, the values of $\delta_{p_{\max}}(x^{(t,h)})$ (see Eq. (2)) for measured data and $R(t,h)$ (see Eq. (5)) for both models are shown. Over- and underestimation is marked in red and blue, respectively. The predicted value that fits best is highlighted in bold.

parameters		# particles	expected velocity /m s^{-1}			objective functions		
t	h	data	data	copula model	RBFN model	data	copula model	RBFN model
25 °C	0 mm	1336	274.9	**274.7**	279.8	0.024	0.071	**0.019**
	10 mm	1054	267.1	**267.0**	273.1	0.033	**0.037**	0.021
	20 mm	898	258.3	**257.0**	263.3	0.006	**0.016**	0.022
	30 mm	778	244.2	**244.7**	243.1	0.0	**0.005**	0.012
	40 mm	686	230.1	**230.1**	232.7	0.0	**0.001**	0.006
	50 mm	713	213.7	**213.2**	229.7	0.0	**0.0**	0.004
100 °C	0 mm	1101	314.2	**314.2**	311.0	0.253	**0.322**	0.149
	10 mm	999	305.4	**305.4**	304.6	0.148	0.225	**0.135**
	20 mm	839	296.3	**294.2**	290.1	0.123	0.148	**0.107**
	30 mm	668	279.3	**280.5**	266.1	0.093	**0.084**	0.039
	40 mm	620	264.4	**264.5**	255.8	0.042	**0.036**	0.017
	50 mm	466	246.8	**246.1**	248.5	0.012	0.009	**0.011**
200 °C	0 mm	520	320.3	**319.7**	323.2	0.478	0.403	**0.428**
	10 mm	507	316.7	**316.9**	319.3	0.325	**0.302**	0.396
	20 mm	531	310.7	**310.1**	311.5	0.283	**0.236**	0.344
	30 mm	528	299.4	**299.3**	293.5	0.271	0.183	**0.292**
	40 mm	540	285.1	**284.4**	279.2	0.162	**0.129**	0.24
	50 mm	455	265.5	**265.5**	275.3	0.182	0.066	**0.186**
75 °C	15 mm	453	309.5	**290.1**	286.0	0.133	**0.127**	0.077

3.2. **Optimization of process parameters**

The good fits of both (copula and RBFN) models stated in Section 3.1 suggest that both models are capable of accurately predicting the values $R(t,h)$ of the objective function given in Eq. (5), even for process parameter vectors (t,h) that were not used for model training, thus allowing optimization of process parameters. In the following we discuss this in more detail.

Table 1 shows (in red and blue) the tendency of both models to slightly over- or underestimate the descriptor $\delta_{p_{\max}}(x^{(t,h)})$ of product quality in the case of no temperature costs ($\alpha = 0$), where it can be observed that the copula model tends to overestimate this descriptor for small temperatures t. However, there is no such clear trend for the RBFN model, which is likely due to the multimodalities occurring for the latter model. Although the copula model predicts the expected particle velocities much better than the RBFN model, see Table 1, this can not be observed when considering the descriptors $\delta_{p_{\max}}(x^{(t,h)})$ and $R(t,h)$ of product quality. Anyhow, for $(t,h) = (75\,°\text{C}, 15\,\text{mm})$, i.e., for validation data the copula model predicts the expected velocity as well as the product quality more accurately than the RBFN model.

In Figure 8, two-dimensional plots of $R(t,h)$ are visualized for $t \in [25\,°\text{C}, 200\,°\text{C}]$ and $h \in [0\,\text{mm}, 60\,\text{mm}]$, where two distinct temperature cost scenarios ($\alpha = 0$ and $\alpha = 10^{-3}$) are considered. On the left-hand side of Figure 8, the values $R(t,h)$ of the objective function given in Eq. (5) are plotted in the case of no temperature costs ($\alpha = 0$). In this case, both models predict that due to the absence of temperature costs, higher temperatures t yield larger values $R(t,h)$ of the objective function. Furthermore, both models indicate that $h = 0\,\text{mm}$ is optimal. As already mentioned in Section 2.1.3, $h = 0\,\text{mm}$ does not refer to the substrate being directly positioned at the nozzle, but rather at the closest feasible point where the HiWatch measuring device can be positioned due to the experimental setup. In fact, particles continue accelerating outside the nozzle until their velocity matches the gas speed and thus a positioning at too close distances would not be feasible even when considering particle descriptors measured in free jets. However, this acceleration occurs in the region where $h < 0\,\text{mm}$, and thus is not reflected in the data.

When temperature costs are introduced ($\alpha = 10^{-3}$), a shift of the optimal solution towards lower temperatures is observed, see Figure 8 (right). In this case, the copula model predicts a lower optimal temperature of about $t = 110\,°\text{C}$, whereas the RBFN model predicts an optimal temperature of about $t = 150\,°\text{C}$. Note that a more precise computation of the optimum is omitted due to the limited precision of the adjustable process parameters. For the optimum ($\alpha = 10^{-3}$) predicted by the copula model, 43% of the mass of particles is predicted to not bond to the substrate, while 38% of the mass bond with a spread greater than $p_{\max}$. In the case of the RBFN model, 42% of the mass of the particles is predicted to fail to bond, and 39% bond with a too high spread. Although these values for both models are quite similar, it is noteworthy that the maximum of the objective function is achieved for a lower temperature in case of the copula model. The resulting optima in relation to the distance of the nozzle outlet to the measuring range of the HiWatch are, as expected, in the range of $h = 0 - 6\,\text{mm}$ and thus in the lower range of the parameter space. The results after the introduction of the temperature cost function show a considerable potential for the energetic optimization of the overall process through the suitable selection of the process temperature t. This not only reasonable from an energy point of view, but also enables the optimum processing of temperature and oxidation-sensitive materials.

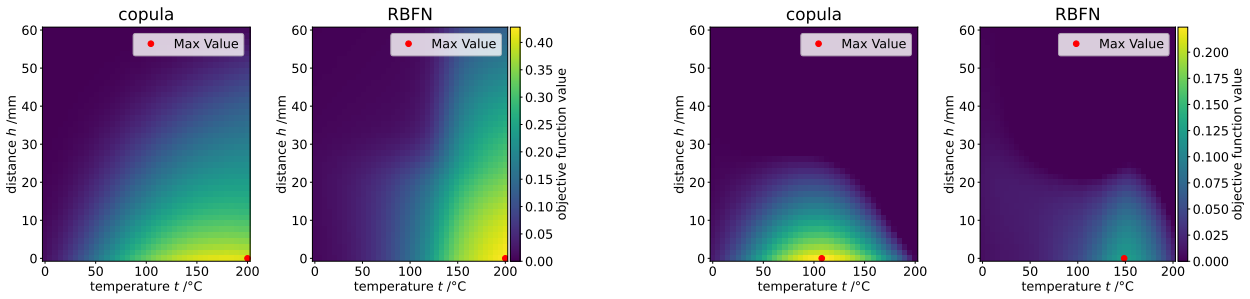

FIGURE 8. Visualization of the values $R(t,h)$ of the objective function given in Eq. (5) for both modeling approaches and for $\alpha = 0$ (left) and $\alpha = 10^{-3}$ (right). The corresponding best process parameters are highlighted by red dots.

The trivariate probability density $f^{(t,h)}_{(V,S,D)}$ of the particle descriptor vector (V, S, D) enables not only to compute the value $R(t, h)$ of the objective function given in Eq. (5) and the expected fraction of bonded particles, but also the prediction of the spatial mass distribution of the particles that bond to the substrate. Figure 9 visualizes these distributions for both models using the validation dataset, where $(t, h) = (75\,°\mathrm{C}, 15\,\mathrm{mm})$. The number-weighted densities shown in Figure 9a are consistent with the observations made in Figure 6. The mass-weighted probability densities in Figure 9b represent the distribution of mass in the jet plume. In Figure 9c, the critical velocity threshold is applied, removing all mass corresponding to particles whose velocities do not exceed this threshold. Consequently, a significant fraction of mass is filtered out, leaving a narrow distribution of particle offsets, which corresponds to the predicted mass distribution on the substrate.

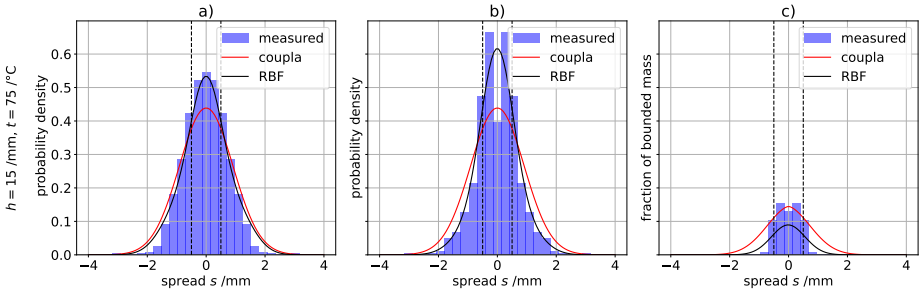

FIGURE 9. Measured and predicted spatial mass distributions of particles that bond to substrate, for the validation dataset, i.e., for $(t, h) = (75\,°\mathrm{C}, 15\,\mathrm{mm})$: number-weighted densities of particle spread (a), corresponding mass-weighted densities (b), and densities of particle spread for particles whose velocity exceeds the critical velocity threshold (c). The dashed vertical lines indicate a spread of $p_{\max} = 0.5$.

4. Conclusion and Outlook

In this study, the applicability of data-driven stochastic modeling approaches for the optimization of the cold gas spray process was investigated. Two different methods were presented, a low-parametric approach based on R-vine copulas and a fast and easy-to-implement approach based on RBFNs. By means of both modeling approaches, we were able to predict the particle velocity distribution for data that was not used for model training. In a simplified setting of a cold gas spraying process, where the critical particle velocity for bonding to the substrate is approximated by the particle velocity measured in the free jet, the models considered in this study can be used to determine optimal process parameters. In particular, these models make it possible to capture the complex dependencies between process parameters and product quality. Furthermore, once calibrated, these models are suitable for autonomous process control due to their small computation times.

In a future study, we will extend the methods proposed in the present work to include further image measurements such as X-ray microtomography, which provides 3D image data of the manufactured product in order to close the gap between free jet measurements and actual particle colliding with the substrate. This allows us to analyze the surface morphology of the particles bond to the substrate. In this way, we can correlate 3D morphological descriptors of the product with free jet particle descriptors to further characterize and quantify the quality of the spraying process. Since the proposed approaches are fully data-driven, the presented methods will be able to capture the influence of the flow field affecting the particle velocity, especially near the nozzle and the substrate. However, in order to model these phenomena and to achieve more realistic optima in terms of the distance of the substrate to the nozzle, further data acquisition is necessary, especially of the experimentally highly complicated case of particle tracking within a non-free jet.

5. Acknowledgement

The authors gratefully acknowledge funding by the German Research Foundation (DFG) within SPP 2364 under grants 504580586 and 504954383.

References

1. Prashar, G. and Vasudev, H. A comprehensive review on sustainable cold spray additive manufacturing: State of the art, challenges and future challenges. *Journal of Cleaner Production* **310,** 127606 (2021).
2. Raoelison, R., Verdy, C., and Liao, H. Cold gas dynamic spray additive manufacturing today: Deposit possibilities, technological solutions and viable applications. *Materials & Design* **133,** 266–287 (2017).
3. Moridi, A., Hassani-Gangaraj, S. M., Guagliano, M., and Dao, M. Cold spray coating: review of material systems and future perspectives. *Surface Engineering* **30,** 369–395 (2014).
4. Thielen, S., Breuninger, P., Hotz, H., Burkhart, C., Schollmayer, T., Sauer, B., Antonyuk, S., Kirsch, B., and Aurich, J. C. Improving the tribological properties of radial shaft seal countersurfaces using experimental micro peening and classical shot peening processes. *Tribology International* **155,** 106764 (2021).
5. Ashokkumar, M., Thirumalaikumarasamy, D., Sonar, T., Deepak, S., Vignesh, P., and Anbarasu, M. An overview of cold spray coating in additive manufacturing, component repairing and other engineering applications. *Journal of the Mechanical Behavior of Materials* **31,** 514–534 (2022).
6. Assadi, H., Kreye, H., Gärtner, F., and Klassen, T. Cold spraying – A materials perspective. *Acta Materialia* **116,** 382–407 (2016).
7. Raoelison, R. N., Verdy, C., and Liao, H. Cold gas dynamic spray additive manufacturing today: Deposit possibilities, technological solutions and viable applications. *Materials & Design* **133,** 266–287 (2017).
8. Villafuerte, J. Recent trends in cold spray technology: looking at the future. *Surface Engineering* **26,** 393–394 (2010).
9. Aleksieieva, O., Dereviankina, L., Breuninger, P., Bozoglu, M., Tretiakov, P., Toporov, A., and Antonyuk, S. Simulation of particle interaction with surface microdefects during cold gas-dynamic spraying. *Coatings* **12,** 1297 (2022).
10. Villafuerte, J. *Modern Cold Spray: Materials, Process, and Applications* (Springer, 2015).
11. Saboori, A., Aversa, A., Marchese, G., Biamino, S., Lombardi, M., and Fino, P. Application of directed energy deposition-based additive manufacturing in repair. *Applied Sciences* **9,** 3316 (2019).
12. Wu, H., Xie, X., Liu, M., Verdy, C., Zhang, Y., Liao, H., and Deng, S. Stable layer-building strategy to enhance cold-spray-based additive manufacturing. *Additive Manufacturing* **35,** 101356 (2020).
13. Papyrin, A., Kosarev, V., Klinkov, S., Alkhimov, A., and Fomin, V. M. *Cold Spray Technology* (Elsevier, 2006).
14. Champagne, V. K. *The Cold Spray Materials Deposition Process* (Woodhead, 2007).
15. Assadi, H., Gärtner, F., Stoltenhoff, T., and Kreye, H. Bonding mechanism in cold gas spraying. *Acta Materialia* **51,** 4379–4394 (2003).
16. Schmidt, T., Gärtner, F., Assadi, H., and Kreye, H. Development of a generalized parameter window for cold spray deposition. *Acta Materialia* **54,** 729–742 (2006).
17. Grujicic, M., Zhao, C., DeRosset, W., and Helfritch, D. Adiabatic shear instability based mechanism for particles/substrate bonding in the cold-gas dynamic-spray process. *Materials & Design* **25,** 681–688 (2004).
18. Wallis, G. B. *One-Dimensional Two-Phase Flow* (McGraw-Hill, 1969).
19. Yin, S., Meyer, M., Li, W., Liao, H., and Lupoi, R. Gas flow, particle acceleration, and heat transfer in cold spray: A review. *Journal of Thermal Spray Technology* **25,** 874–896 (2016).
20. Schmidt, K., Buhl, S., Davoudi, N., Godard, C., Merz, R., Raid, I., Kerscher, E., Kopnarski, M., Müller-Renno, C., Ripperger, S., Seewig, J., Ziegler, C., and Antonyuk, S. Ti surface modification by cold spraying with TiO 2 microparticles. *Surface and Coatings Technology* **309,** 749–758 (2017).
21. Aleksieieva, O., Bozoglu, M., Tretiakov, P., Toporov, A., and Antonyuk, S. Coating of refractory surfaces with fine TiO2 particles via gas-dynamic cold spraying. *Coatings* **14,** 1151 (2024).

22. Czado, C. *Analyzing Dependent Data with Vine Copulas* (Springer, 2019).
23. Furat, O., Leißner, T., Bachmann, K., Gutzmer, J., Peuker, U. A., and Schmidt, V. Stochastic modeling of multidimensional particle properties using parametric copulas. *Microscopy and Microanalysis* **25,** 720–734 (2019).
24. Neumann, M., Gräfensteiner, P., Machado Charry, E., Hirn, U., Hilger, I., Manke, R., Schmidt, V., and Zojer, K. R-vine copulas for data-driven quantification of descriptor relationships in porous materials. *Advanced Theory and Simulations* **7,** 2301261 (2024).
25. Buhmann, M. D. *Radial Basis Functions: Theory and Implementations* (Cambridge University Press, 2003).
26. Poggio, T. and Girosi, F. Networks for approximation and learning. *Proceedings of the IEEE* **78,** 1481–1497 (1990).
27. Wu, Y., Wang, H., Zhang, B., and Du, K. L. Using radial basis function networks for function approximation and classification. *International Scholarly Research Notices* **2012,** 324194 (2012).
28. Wang, Z. and Scott, D. W. Nonparametric density estimation for high-dimensional data—Algorithms and applications. *Wiley Interdisciplinary Reviews: Computational Statistics* **11,** e1461 (2019).
29. Breuninger, P., Krull, F., Buhl, S., Binder, A., Merz, R., Kopnarski, M., Sachweh, B., and Antonyuk, S. Microstructuring of titanium surfaces with plasma-modified titanium particles by cold spraying. *Particuology* **44,** 90–104 (2019).
30. Breuninger, P., Krull, F., Huttenlochner, K., Müller-Reno, C., Ziegler, C., Merz, R., Kopnarski, M., and Antonyuk, S. Microstructuring of steel surfaces via cold spraying with 316L particles for studying the particle-wall collision behavior. *Surface and Coatings Technology* **379,** 125054 (2019).
31. Buhl, S., Breuninger, P., and Antonyuk, S. Optimization of a laval nozzle for energy-efficient cold spraying of microparticles. *Materials and Manufacturing Processes* **33,** 115–122 (2018).
32. Koivuluoto, H., Matikainen, V., Larjo, J., and Vuoristo, P. Novel online diagnostic analysis for in-flight particle properties in cold spraying. *Journal of Thermal Spray Technology* **27,** 423–432 (2018).
33. Schmidt, T., Assadi, H., Gärtner, F., Richter, H., Stoltenhoff, T., Kreye, H., and Klassen, T. From particle acceleration to impact and bonding in cold spraying. *Journal of Thermal Spray Technology* **18,** 794–808 (2009).
34. Gilmore, D. L., Dykhuizen, R. C., Neiser, R. A., Smith, M. F., and Roemer, T. J. Particle velocity and deposition efficiency in the cold spray process. *Journal of Thermal Spray Technology* **8,** 576–582 (1999).
35. Silverman, B. W. *Density Estimation for Statistics and Data Analysis* (Routledge, 2018).
36. McLachlan, G. and Peel, D. *Finite Mixture Models* (J. Wiley & Sons, 2000).
37. Dißmann, J., Brechmann, E. C., Czado, C., and Kurowicka, D. Selecting and estimating regular vine copulae and application to financial returns. *Computational Statistics & Data Analysis* **59,** 52–69 (2013).
38. Joe, H. and Kurowicka, D. *Dependence Modeling: Vine Copula Handbook* (World Scientific, 2019).
39. Held, L. and Bové. *Applied Statistical Inference: Likelihood and Bayes* (Springer, 2014).
40. Johnson, N. L., Kotz, S., and Balakrishnan, N. *Continuous Univariate Distributions* (J. Wiley & Sons, 1995).
41. Nelsen, R. *An Introduction to Copulas* (Springer, 2006).
42. Aas, K., Czado, C., Frigessi, A., and Bakken, H. Pair-copula constructions of multiple dependence. *Insurance: Mathematics and Economics* **44,** 182–198 (2009).
43. Nocedal, J. and Wright, S. J. *Numerical Optimization* (Springer, 1999).
44. Bock, S., Goppold, J., and Weiß, M. An improvement of the convergence proof of the ADAM-Optimizer. *arXiv preprint arXiv:1804.10587* (2018).
45. James, G., Witten, D., Hastie, T., and Tibshirani, R. *An Introduction to Statistical Learning: with Applications in R* (Spinger, 2013).